

Precisely determining photon-number in real time

Leonardo Assis Morais¹, Till Weinhold¹, Marcelo Pereira de Almeida¹, Joshua Combes², Adriana Lita³, Thomas Gerrits³, Sae Woo Nam³, Andrew G. White¹, and Geoff Gillett⁴

¹Centre for Engineered Quantum Systems, School of Mathematics and Physics, University of Queensland, QLD 4072, Australia

²Department of Electrical, Computer and Energy Engineering, University of Colorado Boulder, Boulder, Colorado 80309, USA

³National Institute of Standards and Technology, 325 Broadway, Boulder, Colorado 80305, USA

⁴Quantum Valley Ideas Lab, Waterloo, ON N2L 6R2, Canada

Superconducting transition-edge sensors (TES) are sensitive microcalorimeters used as photon detectors with unparalleled energy resolution. They have found application from measuring astronomical spectra through to determining the quantum property of photon-number, $\hat{n}=\hat{a}^\dagger\hat{a}$, for energies from 0.6–2.33 eV. However, achieving optimal energy resolution requires considerable data acquisition—on the order of 1 GB/min—followed by post-processing, which prevent access to energy information in real time. We report a custom hardware processor to process TES pulses while new detections are still being registered, allowing photon-number to be measured in real time. We resolve photon number up to $n=16$ —achieving up to parts-per-billion discrimination for low photon numbers on the fly—providing transformational capacity for TES applications from astronomy through to quantum technology.

1 Introduction

Superconducting transition-edge sensors (TES) are currently used in wide range of disciplines, with applications ranging from astronomy, where they are used to count photons at the output of a spectrometer [1–3], through to quantum photonics, where output photons are counted in applications that have a known source spectrum [4–9]. TES are single-photon detectors with a set of exquisite properties. These detectors achieve energy resolution of 0.15 eV from the infrared to ultraviolet spectral range [10, 11]; possess an exceedingly low dark count rate—even at low pho-

Leonardo Assis Morais: leoassisfisica@gmail.com

ton flux [12]; and operate with high efficiency—up to 98% [13, 14]. These characteristics combined make TES a photon detector with unique photon-number-resolving (PNR) characteristics (see Table 1 Appendix A for a comparison with other PNR implementations).

Typically, energy information—be it spectrum or photon-number depending on the implementation—is extracted from a TES by measuring the time varying voltage signal produced by each detection event. Usually, the entire data stream from the TES detector output is recorded and post-processed in software [15, 16]. Here, we introduce a different approach: a reconfigurable hardware processor, implemented with a Field-Programmable Gate Array (FPGA), that per-pulse measures and stores a handful of physically significant pulse properties before discarding the voltage signal.

We have implemented a flexible and powerful platform to determine photon-number. Its capabilities include: digitisation of the TES analogue output; identification of pulses related to photon detection events in the digitised data stream; timestamping of detection events; measurement of relevant pulse characteristics to perform photon-number-assignment tasks; and, optionally, recording of the entire pulse, for calibration or cases where optimal information about detection events is required.

2 TES Signal and Analysis

Figure 1a shows 200 detection events for a weak coherent pulse at 820 nm, registered using our hardware processor. After a detection is performed, a sharp rise is observed in the TES output, followed by an exponential-like decay whose constant will depend on the thin film properties

[17, 18]. The sharp rises are of order of hundreds of ns, and the decay time varies from 2 to 8 μ s, depending on the energy of the absorbed photon wavepacket. The higher the number of photons in a detection event, the longer it takes for the detector to cool down to its operating temperature T_0 .

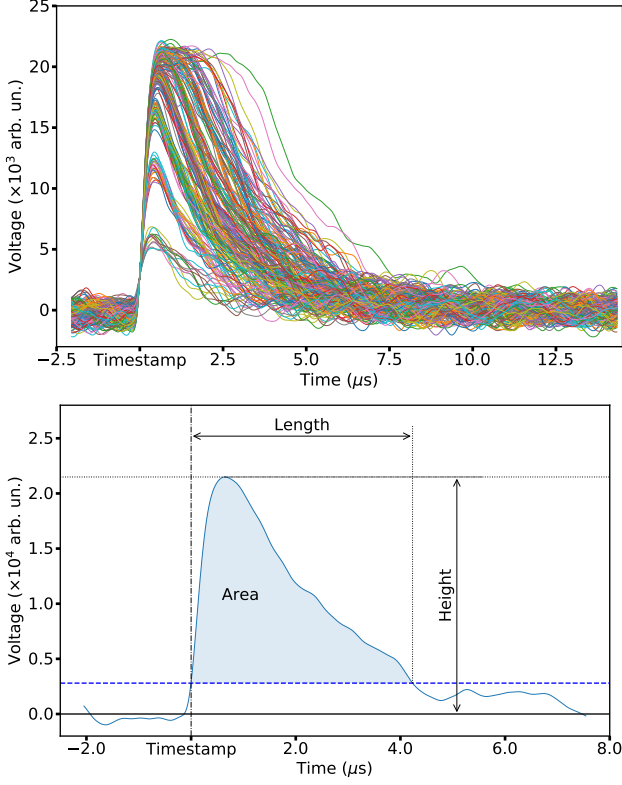


Figure 1: (*Top Panel*) 200 TES pulses captured by our hardware processor using 820 nm pulsed light from a strongly attenuated diode laser. The voltage reading is proportional to the current change due to a photon wavepacket absorption. By keeping the sensor in the transition region between its superconducting and normal phases, we can measure energy with enough precision to distinguish the pulse associated with different photon numbers. (*Bottom Panel*) Single TES pulse digitised by our FPGA showing some of the measurements our system can deliver. The solid black line is the detection baseline and the dash-dotted blue line is the height detection threshold.

Figure 1b highlights the input parameters used to register a valid detection event, and the key characteristics subsequently recorded (see Appendix B for additional characteristics). The user sets: a detection baseline (solid black line) as the reference level with respect to height measure-

ments; the height threshold (blue-dashed line); and the slope threshold (see Figure 6 in Appendix B). To be considered a valid detection event, a TES pulse needs to have both height and slope higher than their respective thresholds. Only when this condition is met are the event packets—structures that gather all the information about the measurements realised—then created and recorded.

To assist the configuration of the baseline and detection thresholds, our processor contains a built-in multi-channel analyser (MCA). The MCA broadcasts in real time histograms of a single quantity of the digitised output from the TES detectors. We use the MCA to analyse the noise levels appropriately and set the baseline and detection thresholds. To determine the position of the detection baseline, we monitor the noise distribution, i.e. the detector output when no light is sent to the detectors. The detection baseline is chosen to be on the mode of the noise distribution. To determine the detection thresholds, we use the same light source which will be used in the experiment. These thresholds are chosen to be in a position between the end of the noise distribution and the first peak related to actual photon detections. Since anything lower than these thresholds will not be considered a valid photon detection event, these parameters will set the effective efficiency of the detections performed. Their appropriate values will depend on the experiment conditions, and a trade off between detection efficiency and background counts must be considered when finding their optimal values.

After setting the baseline and detection thresholds, our system is ready to perform measurements over different characteristics of the TES pulse. By storing only the pulse characteristics instead of the entire pulse, we achieve a 40 times reduction in data transferred and stored. The measured values are available in the FPGA less than 500 ns after the pulse falls below the height threshold. An Ethernet connection transfers pulse data to the computer where photon number information is obtained within milliseconds after registering a pulse event. As TES are limited by their response time to the kHz counting regime, our photon number identification is fast enough to detect events in real time.

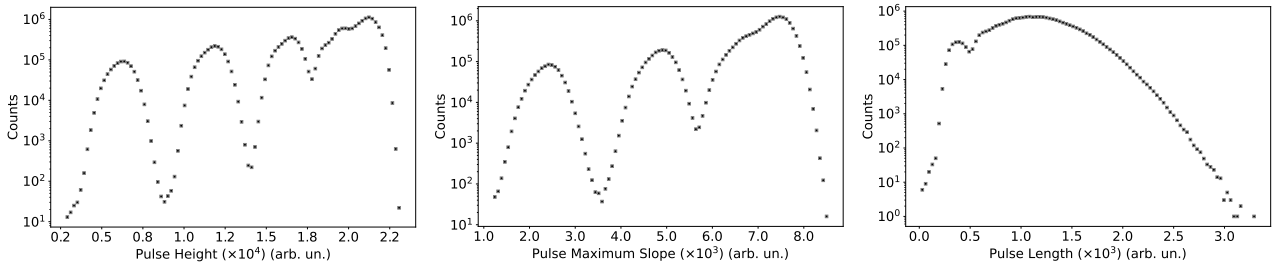


Figure 2: Histograms for photon detection events using a strongly attenuated pulsed diode laser at 820 nm for different aspects of the TES pulse. (*Left Panel*) Height. Up to 3 peaks are clearly resolved. For higher number of photons, the detector undergoes the transition to the normal phase, making it impossible to distinguish photon number using height. (*Middle Panel*) Maximum slope. Only 2 peaks are clearly resolved. We believe that the bandwidth filters used to remove high frequency noise compromise our ability to use pulse slope to distinguish photon number. (*Right Panel*) Length. Due to signal noise, there is poor differentiation between events with 1 or more photons.

3 Detector Calibration

To determine the best way to precisely assign a photon number to a detection event, we measured and analysed four TES pulse characteristics: area, height, length, and maximum slope, as shown in Figure 1b. *Height* is measured as the distance between the baseline and the maximum point in the TES pulse. *Length* is the distance between the rising pulse crossing the detection threshold and the next point where the decaying pulse crosses this threshold again. *Area* is calculated by summing the heights between the detection threshold and the pulse every 4 ns, as shown in the shaded region in the right panel of Figure 1. *Slope* is determined by differentiating the pulse, with the maximum slope being the highest value achieved by the slope signal (see Figure 6 in Appendix B). We show typical histograms for these quantities in Figures 2 and 3. We found that area provides by far and away the best discrimination (as seen in the figures), as well as the highest precision. This reflects the fact that for a TES the pulse area is proportional to the energy absorbed during the detection event—even after the TES undergo the transition to the normal phase occurs [19]—and the TES takes longer to cool down after absorbing a photon wavepacket with higher photon number (see Figure 1a).

Given that a detection event is recorded, what is the chance of assigning a photon number m to a detection event with a true number of n photons? This is the discrimination, and to evaluate it we tested our system using a strongly attenuated pulsed diode laser with emission centred at

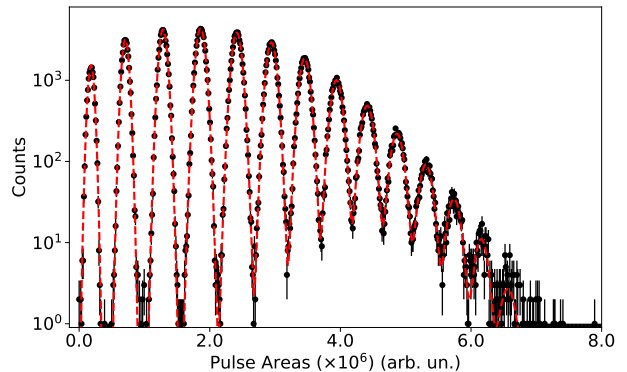


Figure 3: TES Pulse area histogram (black circles) for a strongly attenuated pulsed diode laser at 820 nm. Dashed red line is the model comprised of a sum of 16 Gaussian curves (see Appendix E). There are no peaks associated with 0 photons due to the triggering requirement, as explained in the text. Note that the last 2 Gaussian curves are not visible in the figure due to their low amplitude.

820 nm, described by the weak coherent state:

$$|\alpha\rangle = e^{-|\alpha|^2/2} \sum_{n=0}^{\infty} \frac{\alpha^n}{(n!)^{1/2}} |n\rangle, \quad (1)$$

where $|\alpha|^2$ is proportional to the intensity of the beam.

A series of neutral density filters was employed to attenuate the optical power of our light source. Fine control of the light intensity was achieved by employing a pair of linear polarisers. To guarantee that our source was quasi-monochromatic, we used an 820 nm narrowband filter with 2 nm bandwidth. The light was coupled to a single mode fibre which was directly connected to the TES detectors (see Appendix C for more details

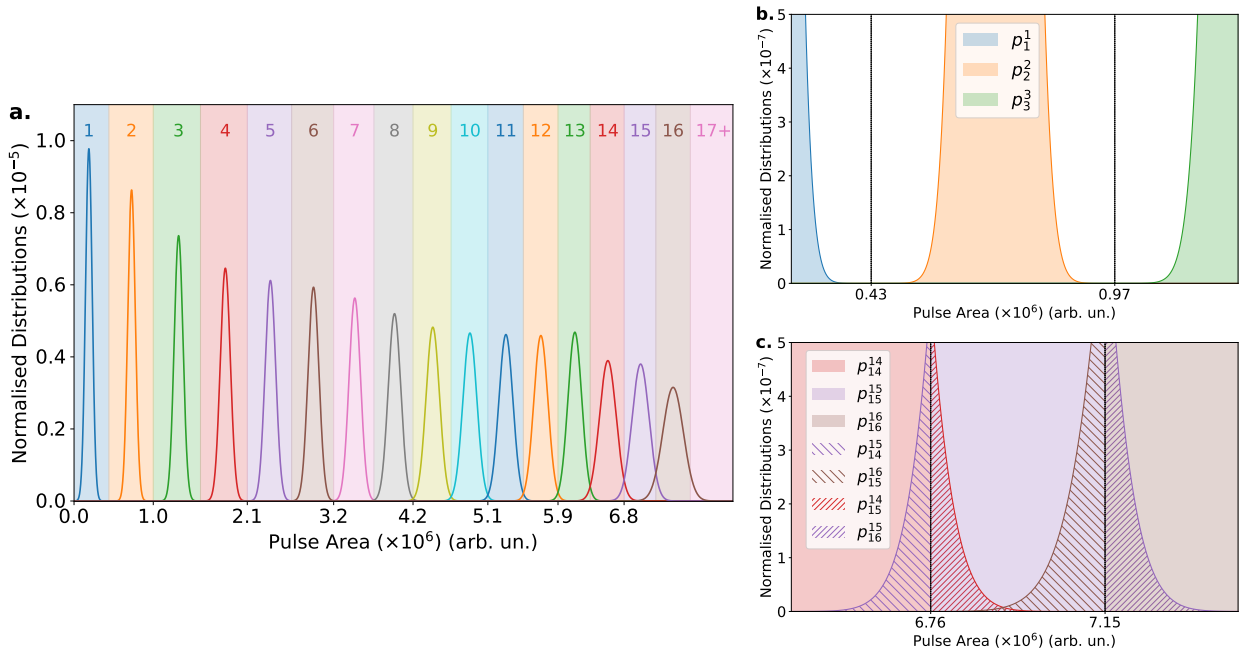


Figure 4: (a) Solid curves are normalised area distributions, $g_n(a)$. The counting thresholds t_m are positioned in the intersection between adjacent distributions. The probability of assigning m photons to a n photon detection event p_m^n is the percentage of area of $g_n(a)$ within a coloured interval $[t_m, t_{m+1}]$. (b)&(c) Insets highlighting the overlaps between three adjacent distributions. (b) Centred at $n=2$, we see $p_2^2=0.9999999527_{(2)}^{(2)}$ (number in parenthesis correspond to one standard deviation), and $p_1^2=8.5 \times 10^{-10}$, $p_3^2=3.88 \times 10^{-9}$. The overlaps between these distributions are too small to be seen in the inset. (c) Centred at $n=15$, we see $p_{15}^{15}=0.936_{(7)}^{(4)}$, and $p_{14}^{15}=2.6 \times 10^{-3}$, $p_{16}^{15}=3.7 \times 10^{-2}$.

about the detectors). Our optical setup was optically isolated to prevent noise contamination. To avoid multi-absorption events (as shown in Figure 8, Appendix D), we used a pulsed light source. The laser was driven with electrical pulses of 2.6 V amplitude and 50 ns width, using a repetition rate of 10 kHz, guaranteeing a time separation of, at least, 100 μ s between subsequent detection events. The TES pulse was amplified at room temperature using a pre-amplifier and differential amplifier, which also applied a 1 MHz bandwidth filter to remove high frequency noise. The filtered signal was digitised by a 14-bit analogue-to-digital converter at a rate of 250 MHz. The digitised signal was the input for our FPGA hardware processor. Our current implementation uses up to two channels simultaneously (see Appendix B for additional details on the FPGA). For further information about the hardware processor implementation, see Ref. [20]. We measured a background count rate of 0.26 ± 0.04 counts/s.

A typical resulting histogram of TES pulse areas is shown in Figure 3 (solid black circles) (see Figure 10 Appendix E for histograms with different intensities). We determined the number of

bins present in the histogram by analysing how the reduced chi-square χ_R^2 varied with the bin number (see Appendix E). Each peak on the TES pulse area histogram is associated with a different photon number. To describe the peaks observed, we used a model composed of a sum of 16 Gaussian curves (red dashed line).

To assign a detection event with pulse area a to a photon number m , we need to determine a set of counting thresholds t_m such that if

$$t_m < a < t_{m+1}, \quad (2)$$

we then assign a photon-number m for this event. These counting thresholds t_m were obtained after normalising each of the distributions obtained through the area histogram analysis. The counting thresholds t_m are positioned in the intersection point between two adjacent normalised distributions, as shown in Figure 4a. Once these t_m are established, assigning photon-number to a detection event becomes a trivial task, which allows us to perform photon-number-resolving measurements in real time. Note that the distributions are wider for larger areas, thus the uncertainty increases when assigning a photon-number to larger

areas.

To evaluate how precisely we can perform these photon-number assignments based on area measurements, we use the normalised distributions as the underlying distributions of photon numbers n registered by the TES in a given detection event. We are interested in determining p_m^n , the probability of correctly assigning the photon-number m to a detection event where n photons were detected. We calculate this probability using

$$p_m^n = \int_{t_m}^{t_{m+1}} g_n(a) da, \quad (3)$$

where $g_n(a)$ is the normalised distribution associated with the detection of photon-number n . In the insets in Figure 4, we select two numbers ($n=2$ and $n=15$) to highlight the overlap between adjacent distributions. Note that for $n=2$ we obtain a precision of parts-per-billion, $p_2^2=0.9999999527_{(2)}^{(2)}$, with the probability of incorrectly assigning a two event to one photon being $p_1^2=8.5\times 10^{-10}$; and for assigning it to 3 photons being $p_3^2=3.88\times 10^{-9}$. For higher photon numbers the discrimination probabilities, p_i^i , gradually reduce, and for 16 photons, we have $p_{16}^{16}=90\%$ (full table in Table 4 in Appendix F). The decrease in discrimination reflects the decreasing counts available: we used a weak coherent pulse such that for $n\geq 13$ there are a relatively small number of counts.

4 Detector Tomography Routine

Our last step to characterise the performance of our detection system was to perform a quantum detector tomography routine [21]. The objective of quantum detector tomography is to reconstruct the positive operator-valued measure (POVM) that completely describes the measurement apparatus [21, 22]. Each POVM element E_m describes a possible detection outcome m . In our case, each E_m describes a measurement result that we associate with a photon-number detection event of m photons. The probability of observing outcome m is given by

$$\Pr(m) = \text{Tr}(\rho E_m), \quad (4)$$

where ρ is the probe state. To perform detector tomography, we need to use a tomographically complete set of input states. For photon-number-resolving measurements, a set of coherent states is

tomographically complete [21, 22]. In our analysis, we used 4 strongly attenuated coherent states $|\alpha\rangle$ with α varying from 1.38 to 2.16 as input states. The values for α were obtained from fitting coherent states to the counts obtained using the calibration method described in section 3.

The experimental setup employed is the same described in section 3, with a 820 nm pulsed diode laser being used as the light source. For all intensities, subsequent pulses are separated by 100 μs time window. For each intensity, we acquired approximately 1.7×10^7 counts. To measure the number of vacuum detections, we used the signal from the electric pulse generator as a reference. We chose a coincidence interval of 600 ns between the TES and generator pulses. A generator pulse without a corresponding TES pulse was considered a vacuum count.

We note that, since TES measures the energy of the photon wavepacket, it is a phase insensitive detector [16, 23]. Therefore, only the diagonal of a POVM element will have non-zero terms, and only the intensity $|\alpha|^2$ of the coherent states is sufficient to characterise the input states. For a coherent state $|\alpha\rangle$, the probability of observing n photons in a detection event is given by

$$\Pr(n|\alpha) = e^{-|\alpha|^2/2} \frac{|\alpha|^{2n}}{n!}. \quad (5)$$

The tomographic routine consists in inverting Equation (4) using the recorded data for $\Pr(m)$ and the known set of input states $\{\rho_i\}$ to determine the set of POVM elements $\{E_m\}$. To obtain the POVM, we performed a two-norm minimisation using the convex optimisation package for Python (CVXPY) [24, 25]. The estimated POVM is the solution to:

$$E_{\text{est}} = \arg \min_E (||\Pr(m) - FE||_2^2), \quad (6)$$

where F is a matrix where the rows represent different α , and the columns represent their projection for different values of m used. $E = E_m$ for $m = [0, N]$ is the detector POVM, where N is the maximum number of photons the detector can distinguish. The POVM element E_N is defined as

$$E_N = \mathbb{1} - \sum_{m=0}^{N-1} E_m, \quad (7)$$

where $\mathbb{1}$ is the identity matrix. E_N accounts for all detection with N or more photons. The con-

straints over the POVM elements E_m are

$$\sum_{m=0}^N E_m = \mathbb{1}, \quad \text{and} \quad E_m \geq 0, \quad (8)$$

to ensure the POVM is physically realisable. The estimated POVM elements $E_{\text{est},m}$ are defined by

$$E_{\text{est},m} = \sum_{k=0}^N \text{Pr}(m|k) |k\rangle\langle k|, \quad (9)$$

where $\text{Pr}(m|n)$ is the probability of reporting m photons given that there were n photons at the input. For an ideal POVM element, $E_n = |n\rangle\langle n|$, we would have $\text{Pr}(m|n) = \delta_{m,n}$ in Equation (9).

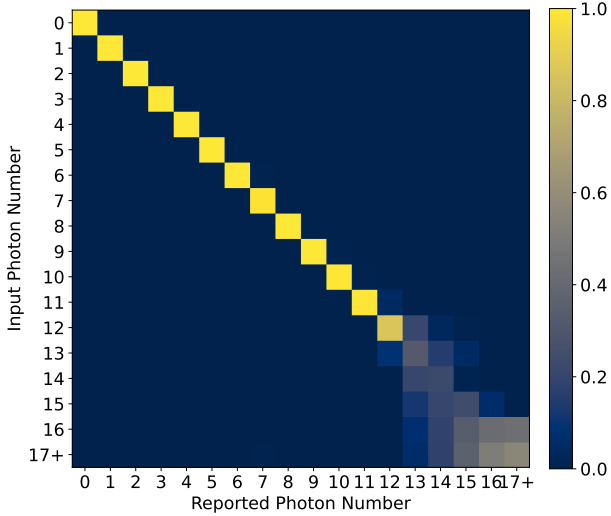


Figure 5: Confusion matrix showing the results for the detector tomography routine. POVM elements are the columns of the confusion matrix, see Equation (9). Colour bar at figure right shows the probability of reporting a photon-number m given an input photon-number n , $\text{Pr}(m|n)$. The quality of reconstruction degrades for $n > 11$ due to the low intensity of the coherent states used in the tomographic routine. We see high quality reconstruction for $n \leq 11$, with $\text{Pr}(m = n|n) \geq 0.99$ in this range.

We show our results using confusion matrices in Figure 5 taking advantage of the fact that all POVM elements are diagonal. Confusion matrices summarise the probabilities of reporting a photon-number m given that you had a detection event with photon-number n , i.e., $\text{Pr}(\text{reported } m | \text{input } n)$. In Figure 5, each column correspond to an estimated POVM element $E_{\text{est},m}$, and each row correspond to an input photon number n . In the ideal case, the confusion

matrix would be the identity matrix, with all terms in the diagonal equal to 1, and all non-diagonal terms 0. We note that the quality of the reconstruction falls considerably for $n > 11$. That is the case even when attempting to reconstruct an ideal POVM with the same input states used in the experimental reconstruction. The limited range of intensities used for the input states and the low number of counts for high photon number limit the reconstruction quality in this range.

The readout fidelity f_{read} provides the average probability of correctly reporting the number of photons in the range analysed, and it is calculated using:

$$f_{\text{read}} = \frac{\text{Tr}(E)}{N}, \quad (10)$$

where N is the maximum number of photons in the interval analysed. $f_{\text{read}} = 0.99$ when analysing the range from 0 to 11 or more photons. When analysing the full range shown in Figure 5, the readout fidelity drops to 0.80, a consequence of the low number of counts in the region where $n \geq 11$. Based on simulations performed with the ideal POVM, we needed to use a set of coherent states covering a broader range of intensities to test the full photon-number-resolving capabilities of our detector. According to our analysis, even in the ideal case we would need to have $\alpha \geq 3.5$, at least, to discriminate up to 17 photons with readout fidelity higher than 0.99.

5 Conclusion

Our FPGA-based hardware processor introduces features desirable across a broad variety of applications. Its parts-per-billion photon-number resolution will allow Gottesman-Kitaev-Preskill (GKP) type optical quantum computing, where the detecting photon-number output pattern is critical [26]. In addition, number resolution shrinks the logical qubit overheads by minimising error rates pushing towards thresholds for fault-tolerant quantum computing [7–9] and is highly desirable in Gaussian BosonSampling [27–29]. The reduction in collected and analysed data from the TES will enable new avenues, such as quantum-enhanced imaging where the ability to have even modest arrays of number-resolving detectors allows imaging maximal information extraction at the quantum limit [30]. Possible applications range from astronomy for imaging

large, remote bodies [30]; to microbiology, where biomolecules can be probed at the single-photon level [31]. The readout of a small array could be handled by a single FPGA-hardware processor, significantly reducing data transfer and storage, as well as the number of data channels.

Acknowledgments

G.G and L.A.M. thanks Lewis Howard for useful discussions. L.A.M. acknowledges the support from the Brazilian Agency CAPES (Coordenação de Aperfeiçoamento de Pessoal de Nível Superior), Finance Code 88881.128437/2016-

01. This research was supported by the Australian Research Council Centre of Excellence for Engineered Quantum Systems (EQUS, CE170100009).

Disclosures

The authors declare no conflicts of interest. Certain commercial equipment, instruments, or materials are identified in this paper to foster understanding. Such identification does not imply recommendation or endorsement by the National Institute of Standards and Technology, nor does it imply that the materials or equipment identified are necessarily the best available for the purpose.

A Comparison with superconducting nanowire single-photon detectors (SNSPD)

Besides TES, SNSPD is a promising technology to deliver photon-number resolving measurements. One of the main techniques to obtain photon number information with SNSPD is to use a series of detectors in a grid, in such a way that the probability of two photons to arrive in the same detector is negligible. In Table 1, we present a comparison of TES with these detectors, taking into account important characteristics, such as: detection efficiency η , dynamic range, wavelength λ range, operating temperature T_O , and count rate.

Detector Type	Dynamic Range, n	Detection Efficiency	T_O	λ range	Count Rate
TES	1 to 16	95%@1550 nm	80 mK	Optical to infra-red	10 KHz
6-Pixel SNSPD [32]	1 to 6	68%@1550 nm	7.0 K	1100 to 2000 nm	300 MHz
24-Pixel SNSPD [33]	1 to 24	0.8%@1310 nm	1.6 K	Not specified	700 MHz

Table 1: Performance comparison between different types of superconducting photon-detectors with photon-number resolving capabilities.

B FPGA Measurements

The FPGA, which performs measurements on the digitised TES signal, is a Xilinx 6 series implemented using the ISE toolchain. From the digitised signal our FPGA derives two signals, as shown in Figure 6: the TES signal (solid blue curve) and slope signal (solid red curve). First, the TES signal is derived directly from the ADC output after it passes a digital low-pass filter, which is used to remove high frequency noise present in the TES pulses. The slope signal is derived from the TES signal using a digital filter configured as a differentiator.

Rises in the data stream are identified using the slope signal: they start when the slope signal becomes positive and finishes when it becomes negative. Once a rise has been identified, it needs to satisfy two conditions in order to be considered a valid detection. First, the maximum slope achieved during a rise must be larger than the slope threshold (dashed red line in Figure 6). Second, the height of the TES signal must be larger than the pulse threshold (dashed blue line in Figure 6). These detection thresholds were introduced in order to allow the hardware processor to distinguish between rises associated to an

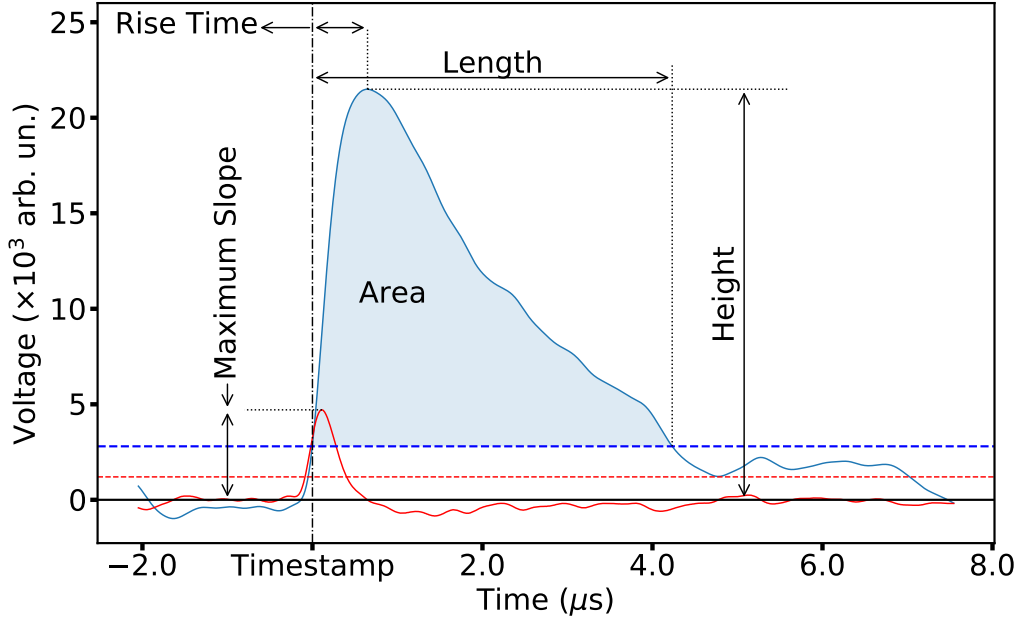


Figure 6: TES pulse detailed with measurements our FPGA can perform. The solid blue line is the TES pulse and the solid red line is the TES pulse slope (amplified 1000 \times for clarity).

actual photon detection from smaller rises due to electronically associated fluctuations of the signal. Both detection thresholds are chosen by the user, based on the information gathered and displayed by the multi-channel analyser, as described in the main text.

From the TES pulse, we also measure the pulse rise time, which is the time taken from the moment the timestamp is given until it reaches the maximum height, as shown in Figure 6. Rise time must be taken into account when considering appropriate coincidence windows for counting coincidences, for example. Additionally, we measure the number of rises in each TES pulse, which can be used to indicate the presence of background counts, for example. The presence of additional rises indicates that two or more absorption events happened before the TES was able to cool down to its operating temperature, as shown in Figure 8. Based on this information, the user can perform a more careful analysis to check if it is possible to assign photon number to different events or to discard the pulse, if the information available is insufficient to assign a photon number with reasonable certainty. We note that height and maximum slope measurements cannot be performed simultaneously in our current implementation.

C TES Detectors

Our TES detectors were fabricated at the National Institute of Standards and Technology (NIST) Boulder, and are thin films of tungsten, with surface area of 25 μm^2 , thickness of 20 nm, fabricated on silicon. NIST reported an efficiency of at least 95% for these detectors [13], in-situ efficiency measurements were not performed. The tungsten thin films are embedded in an optical structure to optimise the absorption at 820 nm wavelength. We use an adiabatic demagnetisation refrigerator (ADR) to maintain the detectors at an operating temperature of 80 mK, below the critical temperature of the tungsten film. The detectors are voltage biased, and after a detection event occurs their initial temperature is restored due to negative electrothermal feedback. The detection circuitry is displayed in Figure 7.

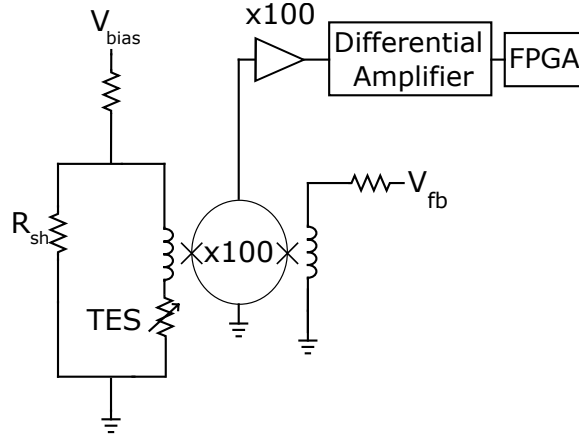


Figure 7: TES bias and readout system. A stable-room temperature current source together with a shunt resistance R_{sh} ($\approx 20m\Omega$) is used to provide the TES voltage bias. When a photon absorption event occurs, the variation in current is amplified using an array of DC superconducting quantum interference devices (SQUID), which are inductively coupled to the TES circuit. These low-noise amplifiers are maintained at $4K$ and amplify the TES signal 100 times. The SQUID output voltage is again amplified a 100 times at room temperature, and then is sent to the differential amplifier. Finally, it passes through an analogue-to-digital converter and is fed to the FPGA where all time and pulse shape measurements are performed. The voltage feedback, V_{FB} is used to bias the SQUIDS.

D Multi-absorption events

TES have no dead time and events with different photons being absorbed at different times can be recorded, as shown in Figure 8. Around $10\mu s$ a second detection event occurs before the detector had enough time to cool down after a first detection had been performed. Our FPGA is able to identify such events by identifying multiple rises in a single detection event and storing the height for different rises. Since multi-absorption events add an extra layer of complexity when performing the photon-number assignment task, in the main paper we used a pulsed light source much slower (10 KHz) than the longest cool down times ($\approx 10\mu s$) to avoid multi-absorption events.

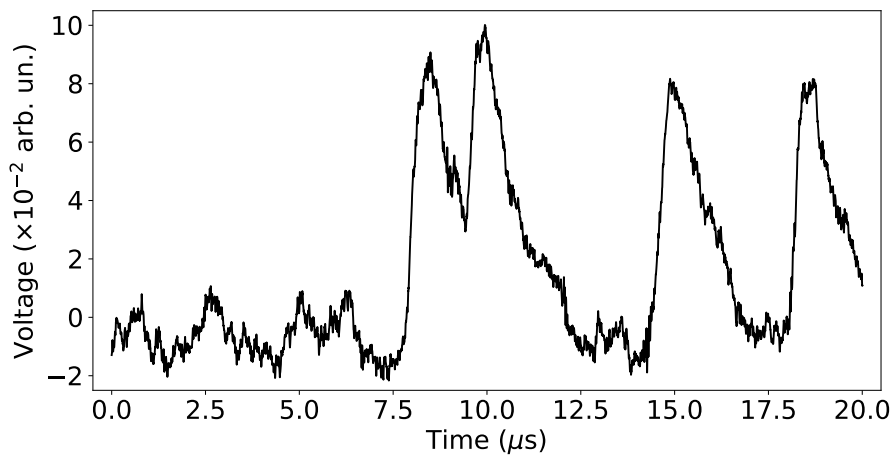


Figure 8: TES analogue output showing a multi-absorption event obtained using an oscilloscope. Our FPGA can identify the multiple rises in a detection event and measure the height of each rise. The user can choose to develop a method to analyse these cases or to remove the events where multi-absorption events occur.

E Area Histogram

The model M we used to fit the area histogram—the dashed red line in Figure 3—was composed of a sum of Gaussian curves $G_n(a)$, defined by

$$M(A_1, \mu_1, \sigma_1, \dots, A_{16}, \mu_{16}, \sigma_{16}) = \sum_{n=1}^{16} G_n(a), \quad (11)$$

where

$$G_n(a) = \frac{A_n}{\sqrt{2\pi}\sigma_n} \exp\left(\frac{-(a - \mu_n)^2}{2\sigma_n^2}\right), \quad (12)$$

with A_n being the amplitude, μ_n the mean, and σ_n standard deviation of the Gaussian used to describe the peak n . To evaluate the goodness of the fit, we used the reduced chi-squared, defined as

$$\chi_R^2 = \sum_i \frac{(C_i - M)^2}{k\epsilon_i^2}, \quad (13)$$

where C_i is the number of counts in the i th bin, ϵ_i is the error in the i th bin, and k is the number of degrees of freedom. We define k by

$$k = n_{bins} - n_{par}, \quad (14)$$

where n_{bins} is the number of bins in the histogram and n_{par} is the number of parameters in the fit. To determine n_{bin} we observed how the χ_R^2 varied as function of the number of bins used, see left panel of Figure 9. To calculate χ_R^2 , we assumed our data followed Poissonian statistics, therefore $\epsilon_i = \sqrt{C_i}$. We choose to divide the analysed area interval of $[0, 10 \times 10^6]$ into 45000 bins, because in this case we obtained $\chi_R^2 \approx 1$. The number of detection events used was, approximately, 1.7×10^7 . The residual Res , shown in the right panel of Figure 9, was calculated using

$$Res_i = \frac{C_i - M}{\sqrt{C_i}}, \quad (15)$$

where C_i is the number of counts in the i th histogram bin.

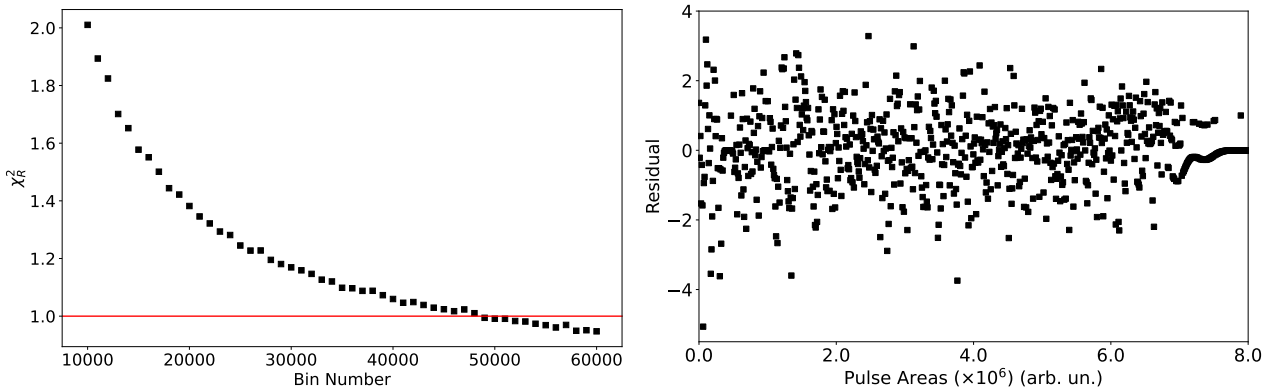


Figure 9: (Left Panel) χ_R^2 for our model M as a function of the number of bins used in the area histogram. (Right Panel) Residual calculated from Equation (15).

To determine the counting threshold position t_m , we used the normalised distributions $g_n(a)$ given by

$$g_n(a) = \frac{1}{\sqrt{2\pi}\sigma_n} \exp\left(\frac{-(a - \mu_n)^2}{2\sigma_n^2}\right), \quad (16)$$

which has area equal to 1.

Once the counting thresholds t_m were established, we calculated the χ_R^2 for each $g_n(a)$ to quantify how well a single Gaussian could describe the data points inside the area interval $[t_m, t_{m+1}]$, see Table 2. Note that for high photon numbers ($n > 14$), the χ_R^2 is smaller than 1. This is an expected result, since this is a low count region, due to the relatively low intensity of the light source used. In Figure 10 we present histograms for different intensities, showing that the intensity of the source can limit the highest number of photons we are able to distinguish using this calibration process.

Peak	χ_R^2	Peak	χ_R^2	Peak	χ_R^2	Peak	χ_R^2
1	2.56	5	1.06	9	1.27	13	1.20
2	0.98	6	1.19	10	1.20	14	0.96
3	2.72	7	1.65	11	1.21	15	0.47
4	1.72	8	1.65	12	1.18	16	0.20

Table 2: Reduced chi-squared, χ_R^2 , between model and data for all peaks. They were calculated by considering the Gaussian distribution $g_n(a)$ used to described a peak in the interval $[t_n, t_{n+1}]$.

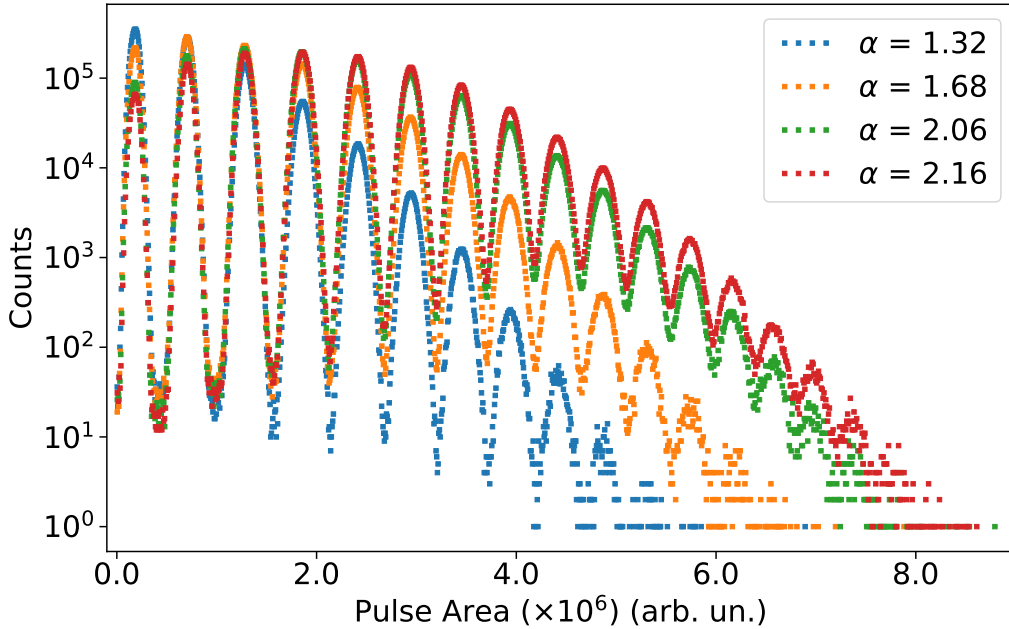


Figure 10: Area histogram for different intensities registered with our detection system. Each color correspond to a different intensity of the light source. Note that the peaks—which correspond to a given photon number—occurs in the same position independent of the intensity used.

To show that this calibration procedure is robust within the intensity range analysed here, we estimated α for a set of 4 different coherent states using different calibrations. Besides the calibration reported in the main paper, we also calibrated the detector using the coherent state with $\alpha = 1.32$ (blue dots in Figure 10). In this case, our model was composed of a sum of 10 gaussian curves due to the lower intensity of the coherent state used for calibration. The counting thresholds t_n were obtained using the same method described above. In Table 3, we compare the estimated values for α for 4 different coherent states using both calibrations. For the left and right tables the value of α for the coherent state used for calibration were 1.32 and 2.16, respectively. Note that for the entire set the α values agree within one standard deviation, showing that our calibration provides consistent estimation for the coherent states used in this low intensity range. We highlight that the standard deviation here presented is the value provided by the fitting algorithm and do not represent the experimental uncertainty with the coherent state used for calibration.

α	σ	χ_{red}^2	α	σ	χ_{red}^2
1.3245	2×10^{-4}	1.18	1.3245	2×10^{-4}	1.22
1.6880	2×10^{-4}	1.18	1.6880	2×10^{-4}	1.24
2.0627	2×10^{-4}	0.88	2.0627	2×10^{-4}	1.81
2.1648	2×10^{-4}	3.88	2.1649	3×10^{-4}	5.33

Table 3: Comparison between estimated values for α using two different coherent states for calibration. For the left table, the coherent state used for calibration had $\alpha = 1.32$. For the right table, $\alpha = 2.16$. We note that all values agree within one standard deviation σ .

F Photon-Number Assignment Probabilities

The discrimination problem: once a photon detection event has been recorded, we would like to determine the number of photons in that event. Table 4 lists the probabilities of correctly, $m=n$, or incorrectly, $m \neq n$, assigning a photon number m to a detection event with n photons, p_m^n . Since only the cases where $m=n-1$ and $m=n+1$ have non-negligible values, we present only these three columns. Note that for 17 photons or more we can no longer discriminate the photon number, therefore p_{17+}^n should be read as the probability of assigning 17 photons *or more* to a detection event which n photons were actually detected. The uncertainties in the probabilities of making a correct assignment $p_{m=n}^n$ were calculated by considering the uncertainties in the position of the detection thresholds t_m . Code available on request.

n	$p_{m=n-1}^n$	$p_{m=n}^n$	$p_{m=n+1}^n$
1	4.01190×10^{-6}	$0.99999598734^{(2)}_{(2)}$	7.5×10^{-10}
2	8.5×10^{-10}	$0.99999999527^{(5)}_{(5)}$	3.88×10^{-9}
3	5×10^{-9}	$0.999999666^{(3)}_{(4)}$	3.31×10^{-7}
4	3.8×10^{-7}	$0.99999343^{(4)}_{(4)}$	6.19×10^{-6}
5	6.6×10^{-6}	$0.9999625^{(2)}_{(2)}$	3.09×10^{-5}
6	3.19×10^{-5}	$0.9998538^{(5)}_{(5)}$	1.142×10^{-4}
7	1.21×10^{-4}	$0.999430^{(2)}_{(2)}$	4.48×10^{-4}
8	4.89×10^{-4}	$0.998007^{(8)}_{(9)}$	1.50×10^{-4}
9	1.63×10^{-3}	$0.99508^{(2)}_{(2)}$	3.28×10^{-3}
10	3.41×10^{-3}	$0.99155^{(3)}_{(4)}$	5.03×10^{-3}
11	5.08×10^{-3}	$0.98840^{(6)}_{(7)}$	6.52×10^{-3}
12	6.6×10^{-3}	$0.9858^{(1)}_{(1)}$	7.6×10^{-3}
13	7.5×10^{-3}	$0.9789^{(7)}_{(7)}$	1.36×10^{-2}
14	1.7×10^{-2}	$0.957^{(2)}_{(3)}$	2.6×10^{-2}
15	2.6×10^{-2}	$0.936^{(4)}_{(7)}$	3.7×10^{-2}
16	5×10^{-2}	$0.90^{(2)}_{(2)}$	5×10^{-2}

Table 4: Probabilities of assigning a photon number m to a detection event with n photons. Middle column is probability of a correct assignment, $m=n$; left and right columns are respectively probabilities of the incorrect assignments $m=n-1$ and $m=n+1$. Upper and lower number in parenthesis indicates the error (one standard deviation) in the reported values for correct probability assignments.

References

- [1] R. W. Romani, A. J. Miller, B. Cabrera, E. Figueroa-Feliciano, S. W. Nam, First Astronomical Application of a Cryogenic Transition Edge Sensor Spectrophotometer, *ApJ* 521 (2) (1999) L153–L156. doi:10.1086/312202.
- [2] J. Burney, T. Bay, J. Barral, P. Brink, B. Cabrera, J. Castle, A. Miller, S. Nam, D. Rosenberg, R. Romani, A. Tomada, Transition-edge sensor arrays for UV-optical-IR astrophysics, *Nucl. Instrum. Methods Phys. Res. A* 559 (2) (2006) 525–527. doi:10.1016/j.nima.2005.12.060.
- [3] S. J. Smith, J. S. Adams, S. R. Bandler, J. A. Chervenak, A. M. Datesman, M. E. Eckart, F. M. Finkbeiner, R. Hummatov, R. L. Kelley, C. A. Kilbourne, A. R. Miniussi, F. S. Porter, J. E. Sadleir, K. Sakai, N. A. Wakeham, E. J. Wassell, Multiabsorber transition-edge sensors for x-ray astronomy, *JATIS* 5 (2) (2019) 021008. doi:10.1117/1.JATIS.5.2.021008.
- [4] J. L. O’Brien, A. Furusawa, J. Vučković, Photonic quantum technologies, *Nat. Photon.* 3 (12) (2009) 687–695. doi:10.1038/nphoton.2009.229.
- [5] R. H. Hadfield, Single-photon detectors for optical quantum information applications, *Nat. Photon.* 3 (12) (2009) 696–705. doi:10.1038/nphoton.2009.230.
- [6] S. Slussarenko, G. J. Pryde, Photonic quantum information processing: A concise review, *Appl. Phys. Rev.* 6 (1) (2019) 041303. doi:10.1063/1.5115814.
- [7] N. Quesada, L. G. Helt, J. Izaac, J. M. Arrazola, R. Shahrokhshahi, C. R. Myers, K. K. Sabapathy, Simulating realistic non-Gaussian state preparation, *Phys. Rev. A* 100 (2) (2019) 022341. doi:10.1103/PhysRevA.100.022341.
- [8] D. Su, C. R. Myers, K. K. Sabapathy, Conversion of Gaussian states to non-Gaussian states using photon-number-resolving detectors, *Phys. Rev. A* 100 (5) (2019) 052301. doi:10.1103/PhysRevA.100.052301.
- [9] I. Tzitrin, J. E. Bourassa, N. C. Menicucci, K. K. Sabapathy, Progress towards practical qubit computation using approximate Gottesman-Kitaev-Preskill codes, *Phys. Rev. A* 101 (3) (2020) 032315. doi:10.1103/PhysRevA.101.032315.
- [10] B. Cabrera, R. M. Clarke, P. Colling, A. J. Miller, S. Nam, R. W. Romani, Detection of single infrared, optical, and ultraviolet photons using superconducting transition edge sensors, *Appl. Phys. Lett.* 73 (6) (1998) 735–737. doi:10.1063/1.121984.
- [11] A. J. Miller, S. W. Nam, J. M. Martinis, A. V. Sergienko, Demonstration of a low-noise near-infrared photon counter with multiphoton discrimination, *Appl. Phys. Lett.* 83 (4) (2003) 791–793. doi:10.1063/1.1596723.
- [12] D. Rosenberg, A. Lita, A. Miller, S. Nam, Noise-free high-efficiency photon-number-resolving detectors, *Phys. Rev. A* 71 (6) (2005) 061803(R). doi:10.1103/PhysRevA.71.061803.
- [13] A. E. Lita, A. J. Miller, S. W. Nam, Counting near-infrared single-photons with 95% efficiency, *Opt. Express* 16 (5) (2008) 3032. doi:10.1364/OE.16.003032.
- [14] D. Fukuda, G. Fujii, T. Numata, K. Amemiya, A. Yoshizawa, H. Tsuchida, H. Fujino, H. Ishii, T. Itatani, S. Inoue, T. Zama, Titanium-based transition-edge photon number resolving detector with 98% detection efficiency with index-matched small-gap fiber coupling, *Opt. Express* 19 (2) (2011) 870. doi:10.1364/OE.19.000870.
- [15] Z. H. Levine, T. Gerrits, A. L. Migdall, D. V. Samarov, B. Calkins, A. E. Lita, S. W. Nam, Algorithm for finding clusters with a known distribution and its application to photon-number resolution using a superconducting transition-edge sensor, *J. Opt. Soc. Am. B* 29 (8) (2012) 2066. doi:10.1364/JOSAB.29.002066.

- [16] P. C. Humphreys, B. J. Metcalf, T. Gerrits, T. Hiemstra, A. E. Lita, J. Nunn, S. W. Nam, A. Datta, W. S. Kolthammer, I. A. Walmsley, Tomography of photon-number resolving continuous-output detectors, *New J. Phys.* 17 (10) (2015) 103044. doi:[10.1088/1367-2630/17/10/103044](https://doi.org/10.1088/1367-2630/17/10/103044).
- [17] B. Calkins, A. E. Lita, A. E. Fox, S. Woo Nam, Faster recovery time of a hot-electron transition-edge sensor by use of normal metal heat-sinks, *Appl. Phys. Lett.* 99 (24) (2011) 241114. doi:[10.1063/1.3659686](https://doi.org/10.1063/1.3659686).
- [18] L. Lolli, E. Taralli, M. Rajteri, T. Numata, D. Fukuda, Characterization of Optical Fast Transition-Edge Sensors With Optimized Fiber Coupling, *IEEE Trans. Appl. Supercond.* 23 (3) (2013) 2100904. doi:[10.1109/TASC.2013.2238981](https://doi.org/10.1109/TASC.2013.2238981).
- [19] K. D. Irwin, An application of electrothermal feedback for high resolution cryogenic particle detection, *Appl. Phys. Lett.* 66 (15) (1995) 1998–2000. doi:[10.1063/1.113674](https://doi.org/10.1063/1.113674).
- [20] G. Gillett, A hardware signal processor for Transition Edge Sensors, PhD Thesis, The University of Queensland (2018). doi:[10.14264/uql.2019.51](https://doi.org/10.14264/uql.2019.51).
- [21] J. S. Lundeen, A. Feito, H. Coldenstrodt-Ronge, K. L. Pregnell, C. Silberhorn, T. C. Ralph, J. Eisert, M. B. Plenio, I. A. Walmsley, Tomography of quantum detectors, *Nat. Phys.* 5 (1) (2009) 27–30. doi:[10.1038/nphys1133](https://doi.org/10.1038/nphys1133).
- [22] A. Feito, J. S. Lundeen, H. Coldenstrodt-Ronge, J. Eisert, M. B. Plenio, I. A. Walmsley, Measuring measurement: theory and practice, *New J. Phys.* 11 (9) (2009) 093038. doi:[10.1088/1367-2630/11/9/093038](https://doi.org/10.1088/1367-2630/11/9/093038).
- [23] G. Brida, L. Ciavarella, I. P. Degiovanni, M. Genovese, L. Lolli, M. G. Mingolla, F. Piacentini, M. Rajteri, E. Taralli, M. G. A. Paris, Quantum characterization of superconducting photon counters, *New J. Phys.* 14 (8) (2012) 085001. doi:[10.1088/1367-2630/14/8/085001](https://doi.org/10.1088/1367-2630/14/8/085001).
- [24] S. Diamond, S. Boyd, CVXPY: A Python-Embedded Modeling Language for Convex Optimization, *JMLR* 17 (2016) 5.
- [25] A. Agrawal, R. Verschueren, S. Diamond, S. Boyd, A rewriting system for convex optimization problems, *JJ. Control Decis.* 5 (1) (2018) 42–60. doi:[10.1080/23307706.2017.1397554](https://doi.org/10.1080/23307706.2017.1397554).
- [26] J. E. Bourassa, R. N. Alexander, M. Vasmer, A. Patil, I. Tzitrin, T. Matsuura, D. Su, B. Q. Baragiola, S. Guha, G. Dauphinais, K. K. Sabapathy, N. C. Menicucci, I. Dhand, Blueprint for a Scalable Photonic Fault-Tolerant Quantum Computer, *Quantum* 5 (2021) 392. doi:[10.22331/q-2021-02-04-392](https://doi.org/10.22331/q-2021-02-04-392).
- [27] C. S. Hamilton, R. Kruse, L. Sansoni, S. Barkhofen, C. Silberhorn, I. Jex, Gaussian Boson Sampling, *Phys. Rev. Lett.* 119 (17) (2017) 170501. doi:[10.1103/PhysRevLett.119.170501](https://doi.org/10.1103/PhysRevLett.119.170501).
- [28] N. Quesada, J. M. Arrazola, N. Killoran, Gaussian boson sampling using threshold detectors, *Phys. Rev. A* 98 (6) (2018) 062322. doi:[10.1103/PhysRevA.98.062322](https://doi.org/10.1103/PhysRevA.98.062322).
- [29] H.-S. Zhong, H. Wang, Y.-H. Deng, M.-C. Chen, L.-C. Peng, Y.-H. Luo, J. Qin, D. Wu, X. Ding, Y. Hu, P. Hu, X.-Y. Yang, W.-J. Zhang, H. Li, Y. Li, X. Jiang, L. Gan, G. Yang, L. You, Z. Wang, L. Li, N.-L. Liu, C.-Y. Lu, J.-W. Pan, Quantum computational advantage using photons, *Science* 370 (6523) (2020) 1460. doi:[10.1126/science.abe8770](https://doi.org/10.1126/science.abe8770).
- [30] L. A. Howard, G. G. Gillett, M. E. Pearce, R. A. Abrahao, T. J. Weinhold, P. Kok, A. G. White, Optimal Imaging of Remote Bodies Using Quantum Detectors, *Phys. Rev. Lett.* 123 (14) (2019) 143604. doi:[10.1103/PhysRevLett.123.143604](https://doi.org/10.1103/PhysRevLett.123.143604).
- [31] K. Niwa, T. Numata, K. Hattori, D. Fukuda, Few-photon color imaging using energy-dispersive superconducting transition-edge sensor spectrometry, *Sci. Rep.* 7 (1) (2017) 45660. doi:[10.1038/srep45660](https://doi.org/10.1038/srep45660).
- [32] X. Tao, S. Chen, Y. Chen, L. Wang, X. Li, X. Tu, X. Jia, Q. Zhao, L. Zhang, L. Kang, P. Wu, A high speed and high efficiency superconducting photon number resolving detector, *Supercond. Sci. Technol.* 32 (6) (2019) 064002. doi:[10.1088/1361-6668/ab0799](https://doi.org/10.1088/1361-6668/ab0799).

- [33] F. Mattioli, Z. Zhou, A. Gaggero, R. Gaudio, R. Leoni, A. Fiore, Photon-counting and analog operation of a 24-pixel photon number resolving detector based on superconducting nanowires, *Opt. Express* 24 (8) (2016) 9067–9076. [doi:10.1364/OE.24.009067](https://doi.org/10.1364/OE.24.009067).